ADVANCED FUNCTIONAL MATERIALS
www.afm-journal.de

Quantifying Electron and Ion Transfers in Contact Electrification with Ionomers

*Xiaoting Ma, Jiaming Zhou, Eunjong Kim, Jingyi Gao, Wenyi Hu, and Dong-Myeong Shin**

Electrostatic charging derived from charge transfer throughout friction is commonplace, but understanding the charge species transferred still remains a debated and contradictory issue. The electron has been widely believed to be the dominant charge carrier for contact electrification between solids, liquids, and gases. However, emerging evidence points to the trait that mobile ions can also contribute to the process, making it more complicated to elucidate even in solid–solid contact electrification. Here, it is demonstrated that electrons and ions concurrently play a role in solid contact-electrification of solid-ionomer pairs, and their contribution differs with environmental humidity levels. The results show that ionic charge transfer can improve contact electrification at high humidity levels of >50% RH. Moreover, adding ions to a non-ionic polymer surface can make contact electrification more resistant to humidity. Overall, the findings highlight the significant role of concurrent electron and mobile ions in contact electrification, although only less than 2% of ions participate in the ion transfer, which can lead to new and improved technologies for electrophotography, electrospraying, energy harvesting, and self-powered sensing.

1. Introduction

Contact electrification, which is electrostatic charging induced by friction, has been ubiquitous and widespread ever since the first documentation in 360 BC,[1] and this phenomenon has been successfully implemented into a broad range of technical applications, including but not limited to electrophotography,[2] electrospraying,[3,4] electrostatic separation,[5] chemical systems[6,7] and energy conversion.[8–18] However, scientific understanding of contact electrification remains relatively in the pioneer stage; in particular, one of the main open questions on what charge species are transferred is still a long-standing and unresolved issue.[19] The obvious suspects of charge species have been electrons,[20–22] ions,[23–27] and material fragments.[28–34] Although some studies insisted that the electron would be a dominant charge carrier for contact electrification between solids, liquids, and gases,[20,35,36] the contact electrification between polymeric materials further complicates the situation. In some previous studies, electrolytic polymers have been found to be transmuted into either charge donors or acceptors through simple ion doping.[37,38] After contact electrification, the polarity of ionomers on the surface has been determined by the tethered ion species within polymers.[24,39,40] Furthermore, even in the absence of embedded ions, the adsorption of water on the surface has been shown to engender forming water ions, serving as a charge carrier in contact electrification.[41] Recent findings highlighting the significance of material fragment transfer[31,32] have intensified the ongoing debate, suggesting that electron transfer may not be the primary mechanism responsible for contact electrification. These pieces of evidence make it difficult to predict the contact electrification by the dominant charge carrier (i.e., electron) transfer alone, as is commonly assumed when establishing triboelectric series.[42,43] Recently, it has been confirmed that ions play a significant role in the solid–liquid contact electrification process,[44] but no research has quantitatively investigated the contributions of electrons and ions in solid–solid systems. Herein, we show that electrons and ions carry the charge simultaneously in contact-electrification of solid-ionomer pairs, in which ion transport is sophisticatedly regulated by anchoring one of the ion species. Both single and multiple friction results indicate that ionic charge transfer is boosted by atmospheric humidity, allowing for significantly enhanced contact electrification at high relative humidity. Moreover, the desired ion implementation onto a non-ionic polymer surface renders the contact electrification of solid/non-ionic polymers more humidity-resistive. Overall, our result points to the significant role of concurrent electrons and mobile ions at the molecular level in the contact electrification process, which can potentially be applicable to designing and optimizing contact electrification for electrophotography, electrospraying, energy harvesting, and self-powered sensing applications.

X. Ma, J. Zhou, E. Kim, J. Gao, W. Hu, D.-M. Shin
Department of Mechanical Engineering
The University of Hong Kong
Pokfulam Road, Hong Kong 999077, China
E-mail: dmshin@hku.hk

The ORCID identification number(s) for the author(s) of this article can be found under https://doi.org/10.1002/adfm.202506471

DOI: 10.1002/adfm.202506471

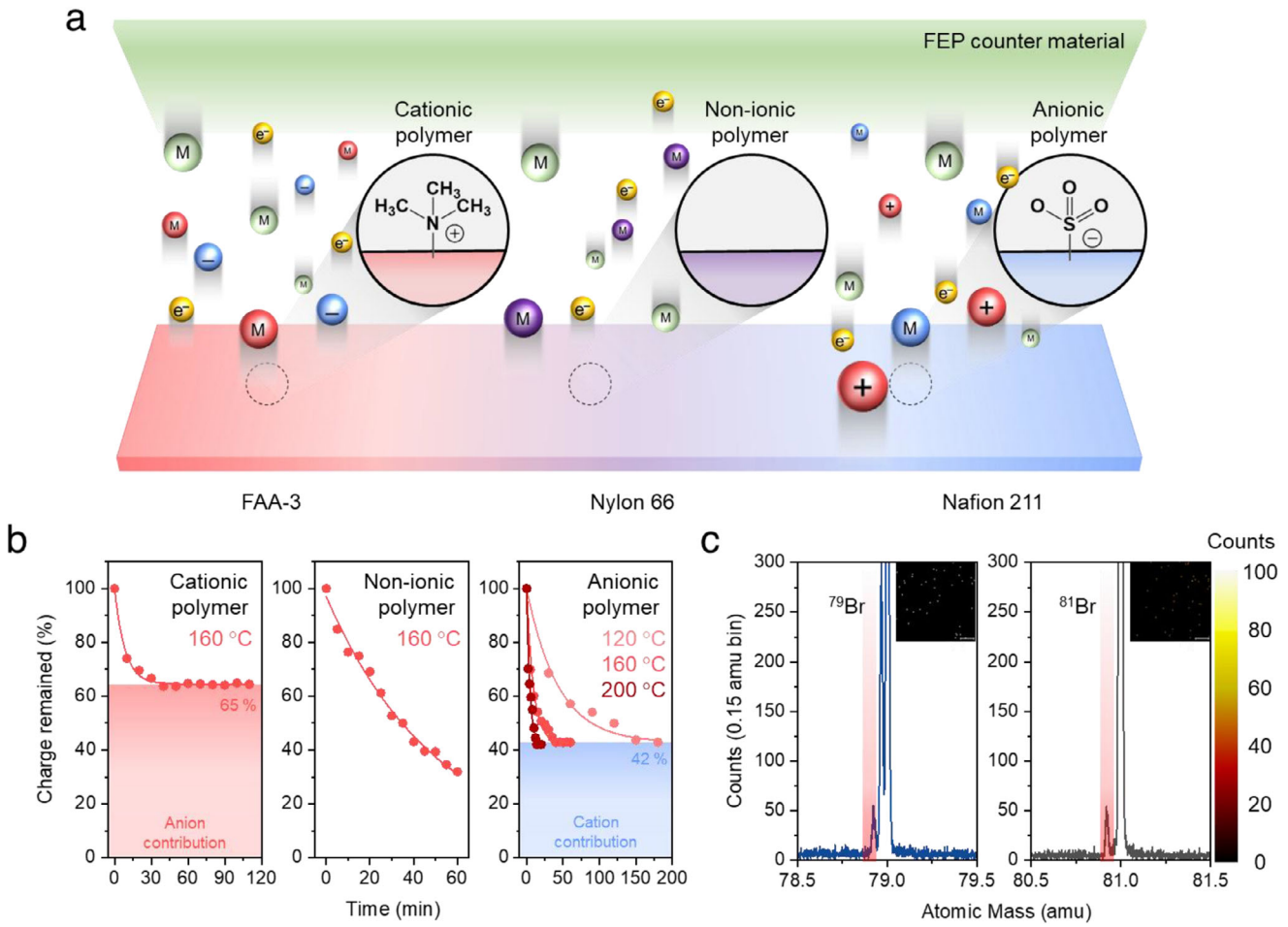

Figure 1. Dual charge carriers in ionomer-solid contact electrification. a), Schematic illustration of charge carriers in ionomers and non-ionic polymer in contact with FEP counter material; electron, anion, and material fragments (cationic polymer, FAA-3), electron and material fragments (non-ionic polymer, nylon 66), and electron, cation, material fragments (anionic polymer, Nafion 211). b), Surface charge retention on FEP rubbed by cationic, non-ionic, and anionic polymers as a function of time at different temperatures (120, 160, and 200 °C). c), Bromide anion transfer into FEP surface after contacting with the cationic polymer confirmed by ToF-SIMS spectrum.

2. Results and Discussion

2.1. Dual Charge Carriers in Solid Contact Electrification

Anionic (Nafion 211) and cationic (FAA-3) polymers embrace physically tethered anions (sulfonate groups) and cations (trimethylammonium groups) into the polymer frameworks, respectively, imposing selective counterion mobility within the polymers (**Figure 1**a; Figure S1, Supporting Information). In addition to the electron and material fragment carriers, mobile ions are able to serve as additional charge carriers at the surface of ionomers during solid contact electrification, so that the electrification in ionomers would be made by electron, material fragment, and ion carriers. As models for multiple charge carrier systems in solid contact electrification, we chose to employ commercially available Nafion 211 (electron and cation), FAA-3 (electron and anion), and nylon 66 (electron, as control) films. Although we use the as-purchased polymeric films, the surface of all polymer films would be supposedly charged by friction over the course of fabrication, transportation, and storage, resulting in being precharged ≈200 μC m^{-2} (Figure S2a, Supporting Information). Prior to all measurements, the precharged surfaces of all samples were first neutralized with a polar solvent (ethanol) three times, followed by mild annealing at 80 °C overnight. The pretreatment facilitated the dramatic surface discharging down to 0.3 μC m^{-2} (Figure S2b, Supporting Information), which was small enough to guarantee reliability in subsequent experiments.

All polymeric materials were brought into contact with a fluorinated ethylene propylene (FEP) film as a counter-friction material at room temperature and 50% relative humidity (RH), and then the charge densities of 100.2, −51.9, and −31.3 μC m^{-2} on FEP surfaces were achieved in contact with anionic, cationic, and non-ionic films, respectively (Figure S3, Supporting Information). The charged FEP films were heated up to the desired temperature in the oven, followed by cooling down to room temperature to determine the remaining surface charge (see Figure S4, Supporting Information for detailed procedure). Figure 1b represents the trace surface charges on FEP film in contact with anionic polymer after annealing at 120, 160, and 200 °C, revealing that the remaining charge density decayed rapidly at higher

Table 1. Surface charge densities induced on FEP surface by ionomers and non-ionic polymer as well as the net electron and ion charge densisties determined at different thermionic emission temperatures.

Polymers	Temperature (°C)	σ_0 (μC m^{-2})	σ_e (μC m^{-2})	σ_s (μC m^{-2})
Anionic polymer	120	100.2	57.3 (57.2%)	42.9 (42.8%)
	160	100.2	57.2 (57.1%)	42.9 (42.8%)
	200	100.2	58.0 (57.9%)	42.2 (42.1%)
Cationic polymer	160	−51.9	−18.3 (35.3%)	−33.5 (64.5%)
Non-ionic polymer	160	−31.3	−29.8 (95.1%)	−0.6 (1.9%)

σ_0, σ_e and σ_s indicate the total surface charge densities on FEP, surface charge density mediated by electrons and surface charge density mediated by sticky charges, respectively.

temperatures and then was saturated at ≈42% regardless of annealing temperature. Similarly, the decay curve for surface charge on FEP film charged by cationic polymer was saturated at ≈65%. In contrast, the FEP film charged by non-ionic polymer was found to show the continuous exponential decay of the surface charge curve after annealing at 160 °C. In order to decouple the contribution of each charge carrier, all decay curves of surface charge (σ(t)) were further fitted by the electron thermionic emission model.[20,44–47]

$$\sigma(t) = e^{-at}\sigma_e + \sigma_s \quad (1)$$

where σ_e and σ_s indicate the surface charge densities mediated by electrons and sticky charges, respectively, while t denotes the decay time. The sticky surface charges of FEP films in contact with anionic and cationic polymers have been shown to be ≈42 and -34 μC m^{-2}, respectively (**Table 1**), quantitatively confirming the existence of additional charge carriers during solid contact electrification. However, the sticky charge on FEP films charged by non-ionic polymer is substantially lower (-0.6 μC m^{-2}), implying that the electron acts as essentially the only charge carrier. Further corroboration of other charge carrier engagement was obtained by the appearance of the characteristic bromine peaks at 78.92 and 80.92 amu on FEP film charged by the cationic polymer in time of flight secondary ion mass spectra (ToF-SIMS (Figure 1c), verifying the mobile ion transfer in solid contact electrification. We performed the quantitative analysis of ToF-SIMS signals to determine the amount of boron transferred from FAA on the FEP surface after multiple contact/separation processes. The atomic concentration (c) ratio of interest species to internal reference is a function of the relative sensitivity factor (RSF) and the intensity (I) of the secondary ion signal, as described in Equation (2).[45–49]

$$C_i/C_r = \left(RSF_i/RSF_r\right)\left(I_i/I_r\right) \quad (2)$$

where the subscripts i and r depict interest species and internal reference, respectively. We chose the fluorine atom as the internal reference, and the signal intensities of fluorine derivatives are presented in **Table 2**. The RSF values of Br and F are very similar,[50] we set $RSF_i/RSF_r = 1$ in this study. The concentration ratio was accordingly determined to be $c_i/c_r = 2.52 \times 10^{-5}$. Assuming ToF-SIMS exhibits the depth resolution of 1 nm from the surface,[51] we extracted the fluorine density in FEP from the molecular dynamics (MD) simulation; the F density is set to be 5.54×10^{18} atoms m^{-2}, and the Br density on FEP surface has been found to be 1.40×10^{14} atoms m^{-2}. Then, the corresponding charge density is -2.23×10^{-5} C m^{-2}, which is comparable to the measured ionic charge density of -3.34×10^{-5} C m^{-2}, suggesting that our method to quantify the ionic charge contribution is reasonable.

We analyzed the Nafion 211 and FAA-3 films using variable-temperature impedance spectroscopy to investigate the energetics of mobile ion conduction (Figure S5, Supporting Information), and the films show activation energies of 1.07 and 0.81 eV, respectively. Given that the potential barrier of electron thermionic emission was reported to be in the range of 0.3–0.8 eV,[20,52–54] the energy barrier for ion conduction is substantially higher compared to that of electrons. These results corroborate the underlying assumption in our method, which is that

Table 2. The intensity of fluorine derivatives and boron in the ToF-SIMS spectrum.

Negative ions	
Derivatives	Intensity
F	6346950
F_2	259594
CF_3	349502
C_2F_3	30071
C_2F_5	156551
C_3F_5	45587
C_3F_7	101007
C_4F_7	20198
Negative F total	**7309460**
Br	**702**
Positive ions	
Derivatives	**Intensity**
CFO	2903
CF_2	385008
CF_3	7274252
C_2F_3	191422
C_3F_3	2380210
C_2F_4	2366557
C_3F_4	701753
C_2F_5	228002
C_3F_5	5195832
C_4F_5	330313
C_3F_7	880144
C_4F_7	701753
C_5F_7	230834
Positive F total	**20546890**

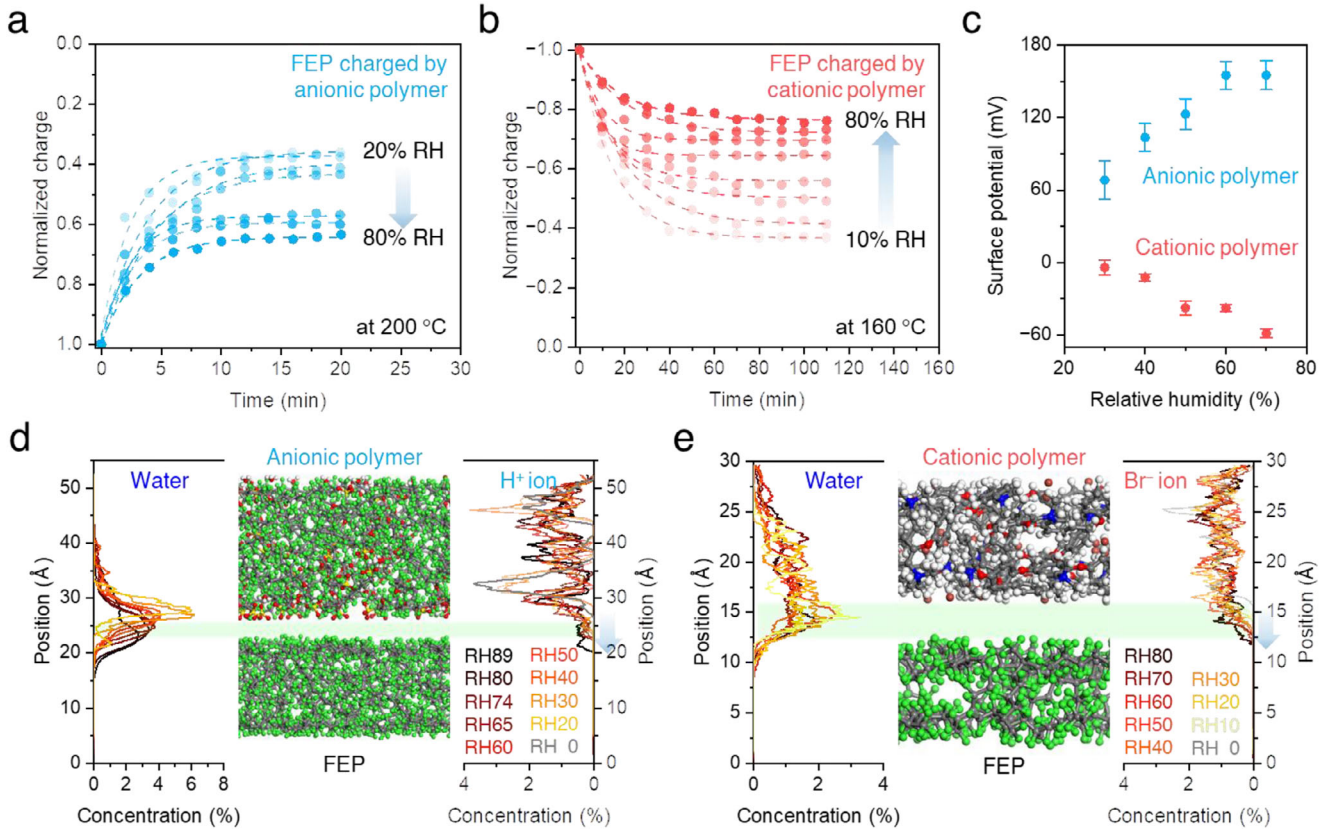

Figure 2. Single contact electrification of ionomers at variable relative humidities. Surface charge retention on FEP contacted with anionic (a) and cationic (b) polymers as a function of time after thermionic emission at 200 and 160 °C, respectively. Each sample was exposed to differing relative humidities in contact electrification. c), Mean surface potential of anionic and cationic polymers at different relative humidities. Data was taken from Figure S9. Computed water and mobile ions distribution within anionic (d) and cationic (e) polymers in the out-of-plane direction. The polymers were exposed to varying relative humidities by tuning the number of water molecules, which was estimated from moisture uptake results in Figure S7.

electrons are quickly emitted from the solid surface as induced by thermionic emission, while ions are rather hard to dissipate from the surface than electrons due to greater binding to atoms on the surface. Moreover, the absence of ammonium and sulfonate derivatives (tethered cationic and anionic groups in ionomers, respectively) on contact-electrified FEP films after 100 cycles of contact-separation helps to exclude the material transfer in the process of contact electrification (Figures S6 and S7, Supporting Information, respectively), which indicates that additional charge carriers would likely be the mobile ions in the solid contact electrification. The surface roughness of polymers – pristine, following a single contact at 9.8 N, and after 20 successive contacts at 9.8 N – was thoroughly characterized utilizing an atomic force microscope (as depicted in Figure S8, Supporting Information). Upon observation, it was discovered that the surface roughness of unprocessed ionomers and their counter-contact polymers counterpart exhibited negligible variance, with the roughness maintaining a consistent pattern even after 20 contact instances. The findings suggest that the inherent smoothness of the surfaces potentially minimizes friction between polymers, providing a plausible explanation for the lack of material transfer observed in our ToF-SIMs results. Given that the inherent surface ionic charge densities of anionic and cationic polymers are estimated to be 2.27 and −1.99 mC m^{-2} (the detailed calculation can be found in Supporting Information), respectively, the transferred cations and anions correspond to 1.9 and 1.7% of the initial charges in anionic and cationic polymers.

2.2. Single Contact Electrification at Variable Relative Humidities

The pendant ionic groups endow ionomers with a hygroscopic nature (Figure S9, Supporting Information), and the hydration of mobile ions derived by moisture uptake determines the ion diffusion across the interface; therefore, atmospheric humidity is a critical factor in determining the ionic transfer contribution to solid contact electrification. We sought to delve into ionic triboelectrification on ionomers at differing relative humidities, and the thermionic emission plots of FEP films charged by anionic and cationic polymers in the RH range of 10% to 80% were presented in **Figure** 2a,b, respectively. An ionic triboelectrification contributions of 35.6 and 41.3% were achieved at 20% RH, and increasing RH gave rise to the ionic contribution to rise up to the highest values of 64.2 and 76.5% at 80% RH for anionic and cationic polymers, respectively (Figure S10, Supporting Information). We attribute humidity-dependent ionic triboelectrification to the greater tendency of mobile ions to dissociate from tethered ionic groups upon hydration at higher RHs, facilitating ion

diffusion through the water bridges formed between two surfaces. We also prepared the Nafion 211 with lithium cations and FAA-3 with chloride anions using ion exchange, and we characterized their sticky charge after a single contact with FEP film as a function of relative humidity. The ion-exchanged analogous exhibited a significant inter-material ion contribution with a similar trend as a function of relative humidity (Figure S11, Supporting Information). We note that the inter-material ion transfer remains similar regardless of the ion species involved as the ion transfer is limited given that the ions can be coordinated with up to ≈3–4 water molecules only even at 80% RH (Figure S9, Supporting Information). We note that the presence of surface water may alter the adhesion on polymeric surfaces, likely resulting in the accumulation of adsorbates[55] or the heterolytic covalent bond cleavage during the material separation.[56] However, in this study, we reset charging acquired during a sample's history by cleaning and baking before the experiments (Figure S2, Supporting Information), and we found no clear evidence of tethered ionic group derivatives transferred to the counter material (Figures S6 and S7, Supporting Information), which together makes us rule out the implication of adsorbates and material transfer over the course of contact electrification. Quantifying such charge carrier contributions in our studies points to the clue that the predominant charge carrier can be altered by the ambient conditions, suggesting that we may customize the materials with a different design rule in order to optimize contact electrification based on the specific working environment. To investigate the presence of surface mobile ions on the ionomers, we scanned the surface potential of the ionomers at differing RHs using Kelvin probe force microscopy. The mean surface potential of anionic polymer exposed to each RH for 30 min increased with elevated RH whereas an increased RH leads to a decrease in the mean surface potential of cationic polymer (Figure 2c; Figure S12, Supporting Information), revealing that more mobile ions are engendered on the surface of ionomers with increasing humidity due to more significant solvating effect.

The binding energies of mobile cations and anions to ionomers at differing RHs were calculated using density functional theory. Protons have been found to strongly coordinate with anionic polymers in the absence of water (binding energy of 315.1 kcal mol^{-1}), but the introduction of water in the vicinity of anionic polymer significantly lowers the binding energy down to 115.0 kcal mol^{-1}, as shown in Figure S13 (Supporting Information). The binding energy of Br^- anions to cationic polymers also becomes lower against increasing humidity, lengthening the anions-polymers pair distance. MD simulations were employed to gain further insight into the mobile cations and anions environments at the interface, and the results are presented in Figure 2d,e. When exposed to the relevant humidity, the hygroscopic ionomers were hydrated and the enhanced segmental mobility of ionic groups facilitated the gap of some portions to reduce below 2 Å. The water concentration profile (left in Figure 2d,e) revealed that the water absorbed was significantly localized at the surface gaps (18–33%) for differing humidities, helping to build the continuous water channels (Movie S1 and Figure S14, Supporting Information). Such channels apparently enable the mobile ions to diffuse onto the surface of the FEP surface; indeed, the ion concentration profiles (right in Figure 2d,e) shifted down ≈1–3 Å toward the counter material in the presence of atmospheric moisture so that the ions were able to reach the surface of FEP by diffusion driven by concentration gradient. The diffusion coefficient toward the out-of-plane (D_z) direction has been shown to elevate with increasing relative humidity (Figure S15, Supporting Information); a low relative humidity (20% RH) resulted in the low out-of-plane relative diffusions of 0.45 and 0.27 $Å^2$ ns^{-1} for the anionic and cationic polymers, respectively, and these values reached up to 1.6 and 1.7 $Å^2$ ns^{-1} for the anionic and cationic polymers at high relative humidity, respectively. A combination of simulation studies implies that the confined water molecules between polymers in the presence of atmospheric moisture form the water channels, facilitating ion diffusion across the interface.

Our single friction results in Figure 2 suggest that both the electron and ion transfers on the ionomer surface occur simultaneously at the single friction. The amount of electron transfer in each friction is supposed to relate to the difference in the occupied energy levels of electrons in the electron cloud model,[35] while the ion transfer would likely be dictated by mobile ion concentration gradient. The ionomers include both the ionic and non-ionic groups structurally (see Figure S1, Supporting Information) so that both groups are subject to contact with counter-contact materials simultaneously. Such a distinct nature in ionomer leads to concurrent electron and ion transfers even at the single friction, which is apart from the solid–liquid contact electrification where electron transfer at the very first contact yields the charged solid surface, and then the charge carried by ions becomes dominant from the second contact.[35]

2.3. Contact Electrification upon Multifriction

Along with the contact electrification derived by the single friction, the charge transfer behaviors upon multifriction must be considered for the practical applications of contact electrification. Regardless of the nature of the charge transfer, the charges transferred on the counter material surface are expected to reach saturation upon multifriction as both the occupied energy levels of electrons and mobile ion concentration would be equalized eventually. The surface charge densities of FEPs contacted with ionomers and non-ionic polymer over the cycles of friction at 20% RH are shown in **Figure 3**a, and there is an obvious saturation process of the surface charge density for all systems. We adopted an empirical model to fit our experimental results, as described in Equation (3):[57]

$$\sigma = \sigma_0 exp\left(-\frac{n}{n_0}\right) + \sigma_\infty \left\{1 - exp\left(-\frac{n}{n_0}\right)\right\} \quad (3)$$

where σ_0 and σ_∞ are the surface charge densities before triboelectrification and after infinite multifriction, respectively. The n and n_0 denote the number of friction and the charge saturation constant, respectively. The experimental results fit very well with the model, and the constants extracted from the fitting are presented in **Table 3**. Interestingly, n_0 becomes substantially greater when ion transfer gets involved, which we attribute to the relatively stronger binding of the ions than the electrons on the ionomer surface, leading to delayed saturation.

Next, we investigated the saturated surface charge densities of FEPs in contact with ionomers and non-ionic polymers exposed

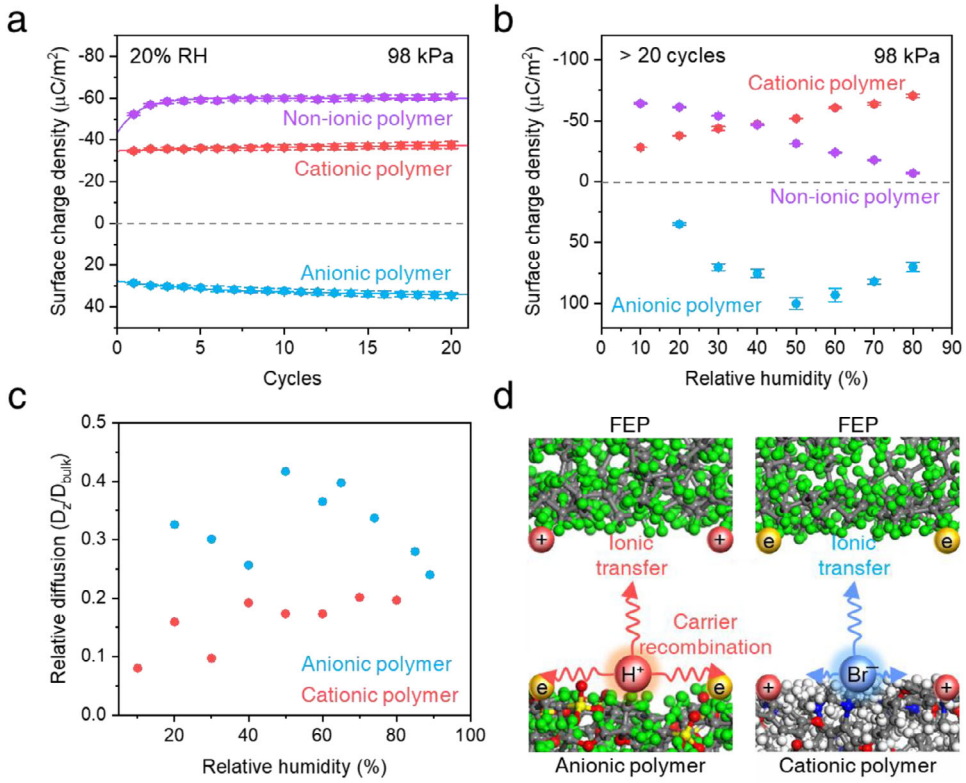

Figure 3. Multifriction electrification in ionomers. a), Surface charge densities on FEP layer in contact with non-ionic, anionic, and cationic polymers over the course of compression/release cycles. b), Saturated surface charge densities on FEP layers charged by non-ionic, anionic, and cationic polymers as a function of relative humidity. c), Relative out-of-plane diffusion of protons and bromide anions in anionic and cationic polymers. d), Schematic of a plausible scenario for mobile ion migration on the surface of ionomers at high humidities. The improved in-plane diffusion of protons at high humidities may result in charge recombination while the bromide anion diffusion still remains anisotropic.

to varying relative humidities (Figure 3b). The surface charge density of FEP in contact with non-ionic polymers becomes less with increasing relative humidity, which is likely due in large part to the electron charge screening by the adsorbed water molecules on the surface. In sharp contrast, as for FEP contacted with the ionomers, the saturated surface charge density is substantially elevated with increasing relative humidity; the surface charge density of FEP contacted with the cationic polymer is −28.1 μC cm^{-2} at 10% RH, increasing to −70.6 μC cm^{-2} with 80% RH, whereas the FEP rubbed with the anionic polymer exhibits the maximum value of 100.2 μC cm^{-2} at 50% RH. We attribute the surface charge enhancement at high humidities to the boosted ion charge contribution together with the spurred mobile ion diffusion. It is noteworthy that the relative out-of-plane anion diffusion (D_z/D_{bulk}) in cationic polymer, which is defined as diffusion toward the out-of-plane (D_z) direction normalized by all directions, has been shown to gradually elevate with increasing relative humidity (Figure 3c), but the relative cation diffusion of anionic polymer has been found to reach the maximum value at 50% RH. These relative diffusion behaviors suggest that the in-plane cation diffusion throughout the anionic polymer surface induces charge carrier recombination, slightly lowering the saturated surface charge density at over 50% RH (Figure 3d).

Table 3. Surface charge densities and charge saturation constants of FEP surface electrificated by ionomers and non-ionic polymers.

Polymers	σ_0 (μC m^{-2})	n_0	σ_∞ (μC m^{-2})
Non-ionic polymer (Nylon 66)	−43.2±1.5	−34.7±0.2	−59.9±0.1
Anionic polymer (Nafion 211)	27.6±0.3	6.4±0.9	34.2±0.3
Cationic polymer (FAA-3)	−34.7±0.2	9.7±3.9	−37.6±0.6

σ^0 and σ^∞ are the surface charge densities before triboelectrification and after infinite multifriction, respectively. n^0 denotes the the charge saturation constant.

2.4. Output Performance in Triboelectric Nanogenerator Devices

We investigated the practical performance of ionomers as contact electrification layers in the triboelectric nanogenerator (TENG) devices featuring an ionomer layer on the Cu electrode separated by a 20 mm gap with an FEP layer on the Cu electrode. The voltage outputs obtained with relative humidity swings between 50% and 80% are shown in Figure 4a–c. The TENG with an FEP/nylon 66 (non-ionic polymer) combination exhibits a decrease of 79.9% in output voltage at high humidity (**Figure 4a**), while the attenuation of the output voltage is reduced to 53.2% in TENG with an FEP/Nafion 211 (anionic polymer) combination (Figure 4b). In particular, the output voltage even increases

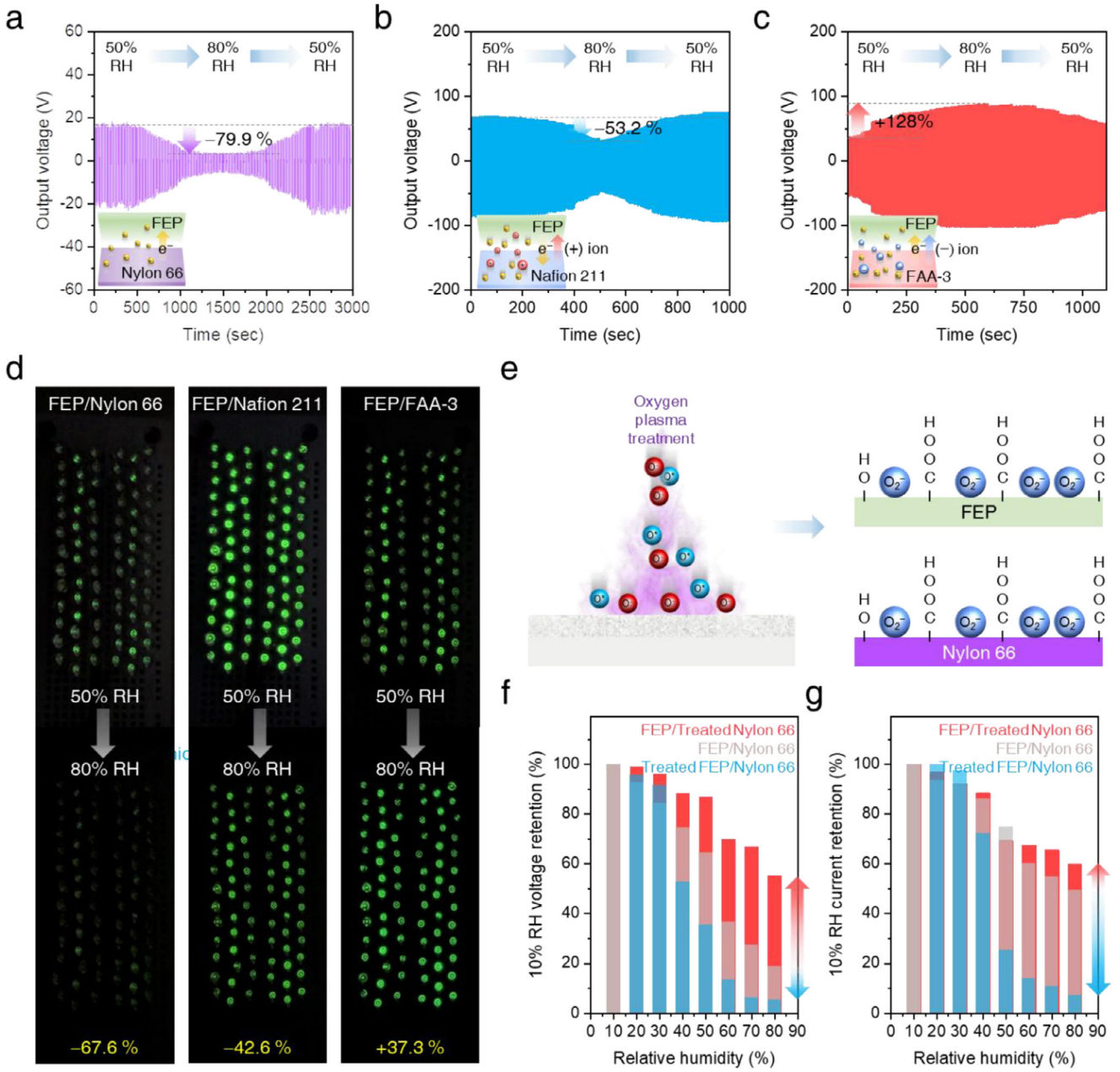

Figure 4. Functionality of ionomers in triboelectric nanogenerators. The voltage outputs arisen from TENGs featuring nylon 66 (a, non-ionic polymer), Nafion 211 (b, anionic polymer), and FAA-3 (c, cationic polymer) contact electrification layers at variable relative humidities from 50 to 80%. d, The snapshots of 78 LEDs lit by TENGs at 50 and 80% RHs. e, Schematic of additional ion injection onto polymer surface using oxygen plasma treatment, facilitating to the formation of hydroxyl and carboxyl groups together with excessive superoxide ions on the non-ionic polymer surfaces. Output voltage (f) and current (g) retentions compared to 10% RH of TENGs comprising FEP/nylon 66, treated FEP/nylon 66, and FEP/treated nylon 66 pairs as a function of relative humidity.

up to 128% with an FEP/FAA-3 triboelectrification layer in TENG (Figure 4c). Electrical energy collected by the periodic compress-release motions was utilized either to power the 78 light-emitting diode (LED) arrays (Figure 4d) or to charge a 10 μF capacitor (Figure S16, Supporting Information). To quantify the brightness of the LED arrays, we employed a custom-built LED analysis application where the 8-bit RGB color components are extracted from the snapshots of videos taken by the mobile phone, and the perceived brightness (PB) of each LED was calculated by the equation:[58]

$$PB = \sqrt{0.299R^2 + 0.587G^2 + 0.114B^2} \quad (4)$$

where R, G, and B are the values of RGB color components in scales 0–255, respectively. The average PB of LEDs powered by the TENG with the FEP/nylon 66 significantly decreases from

71.3 to 23.1 (-67.6%) with increasing RH from 50% to 80%, while the TENG comprising the FEP/FAA-3 shows remarkably the increase in average PB of LEDs from 91.1 to 125.1 (-37.3%) with elevating RH (Figure S17, Supporting Information). Impressively, the TENGs with the ionomer contact electrification layer stably delivered the power even in high humidity. It is important to note that ionic triboelectrification compensates for electron charge screen in higher RHs even if there is a clear tradeoff between electron charge transfer and relative humidity, demonstrating that ionic charge transfer renders the solid–solid contact electrification the humidity-resistive. Long-term stability of ionomer-featured TENG was performed over the 2000 compression-release cycles at 80% RH, as shown in Figure S18 (Supporting Information), indicating the sustainability of ionic triboelectrification.

Beyond the ionomers in which the mobile ions get inherently involved during contact electrification, the addition of mobile ions on the polymer surface may empower the non-ionic polymers to possess strong resistance to higher RHs. We sought to introduce excess anions on the polymer surface using oxygen plasma treatment as portrayed in Figure 4e. Both FEP and nylon 66 films were treated with oxygen plasma for 2 min with a power of 180 W, engendering hydroxyl and carboxyl groups together with excessive superoxide ions on the polymer surface. We constructed the TENGs featuring pristine FEP/pristine nylon 66, treated FEP/pristine nylon 66, or pristine FEP/treated nylon 66 pairs. Given that nylon 66 is an electron donor compared to FEP in the triboelectric series,[59] the electron and ion charge transfers will be desynchronized and synchronized in the treated FEP/pristine nylon 66, or pristine FEP/treated nylon 66 pairs, respectively (Figure S19, Supporting Information). When implementing the synchronized charge transfer, ≈55% and 60% of the voltage and current outputs are retained at 80% RH, respectively, whilst most of the outputs are dramatically diminished when employing the desynchronized charge transfer (Figure 4f and 4g). The decay curves of surface charge over the time after annealing at 160 °C display that ion charges on the FEP sides after the contact electrification between pristine FEP/nylon 66, treated FEP/pristine nylon 66, and pristine FEP/treated nylon 66 pairs are 1.9, 6.9, and 41.6% of total surface charge (Figure S20, Supporting Information), respectively, suggesting that the oxygen plasma treatment is able to afford ion transport in solid–solid contact electrification. To check the formation of superoxide ions, hydroxyl, and carboxyl groups on plasma-treated polymers, ToF-SIMS was used to characterize the polymer surface after O_2 plasma treatment. The bismuth primary ion source was employed for the measurement, helping to rule out the oxygen contamination of the polymer surface from the primary ion source. After plasma treatment, we can obviously observe the distinct peaks of superoxide ions (Figure S21a–c, Supporting Information), hydroxyl groups (Figure S21d–f, Supporting Information), and carboxyl groups (Figure S21g–i, Supporting Information), supporting the formation of such ions and functional groups. We note that decorating additional electron-withdrawing or -donating groups on the polymer surface may be able to alter the electron transfer, and resultingly improve the overall charge transfer. Therefore, we measured the portion of the sticky charge on the surface charge after synchronized charge transfer occurred (Figure S22, Supporting Information). We clearly observed that the sticky charge contribution was 3.3% at 10% RH, and the ionic contribution rose to the highest value of 30.1% at 80% RH as RH increased, indicating that inter-material ion transfer has been found in O_2 plasma-treated polymers.

Indeed, our device demonstration with the ion-introduced polymers represents a proof-of-concept of the fact that the ion injection on the polymer surface in tandem with the synchronized electron and ion charge transfer gives rise to humidity resistance, indicating further room for output optimization of our approach to developing humidity-independent triboelectrification. The synchronized transfer can also be demonstrated in a dual ion charge carrier system with an FEP/marinated electrolyte pair (Figure S23a, Supporting Information). All charge species are expected to move in the same direction, but the lithium transference number, representing the fraction of the current carried by the lithium cation, of polyvinyl alcohol (PVA) film with 1 M LiCl indicates that the chloride anions move at least four times faster than lithium cations (Figure S23b, Supporting Information) so that the dominant ionic charge transfer would occur by anions. As the synchronized charge transfer is happening, the surface charge density on FEP film dramatically increases as a function of RH (Figure S23c, Supporting Information), especially greater than 40% RH, supporting that the synchronized mechanism occurs for dual ion charge carrier systems.

Apart from inter-material ionic charge transfer, the ionic charge retaining is necessary to be taken into account to boost the contact electrification performance effectively. We exerted hydrophilic nylon and PVA films as counter-contact material (Figure S24a, Supporting Information), in which the thin water layer is supposed to be formed on the film surface when exposed to the ambient air,[60] leading to charge dissipations through ion diffusion laterally and vertically on the film surface. Indeed, significant degradation in surface charge has been found as a function of RH even though the synchronized mechanism occurs (open symbols in Figure S24b,c, Supporting Information), and blocking such ion diffusion with the help of hydrophobic surface functionalization (Figure S24d, Supporting Information) remarkably improves surface charge retention at high relative humidities, especially for nylon (solid symbols in Figure S24b,c, Supporting Information), corroborating that control over ion diffusion on the polymer surface after inter-material ion transfer is a critical factor in optimizing the contact electrification.

3. Conclusion

In summary, we have reported the concurrent existence of both electron and ion transfers in solid-ionomer contact electrification, in which the transfer of non-dominant charge species has been generally overlooked in triboelectric society. Thermionic emissions of the surface charge, together with surface imaging mass spectroscopy, reveal that significant ion transfer is engaged in solid-ionomer contact electrification. The contribution of ionic triboelectrification increases with relative humidity, and this trait is especially advantageous given that the tradeoff between electron charge transfer and relative humidity dramatically diminishes the triboelectric performance, rendering the solid-ionomer contact electrification the humidity resistive. Ion injection to non-ionic polymer surfaces helps to implement ion transfer in solid–solid contact electrification, demonstrating that

synchronized charge transfers enable less humidity-sensitive contact electrification. It is noteworthy that the ion transfer contributes significantly to the process of contact electrification, especially at high humidity, although only less than 2% of ions participate in the ion transfer, suggesting that there is room for further performance improvement of contact electrification. Our finding not only suggests that control over ion transfer in solid–solid contact electrification can be a critical factor in designing humidity-insensitive triboelectrification materials, but also provides further insight into the physics behind contact electrification.

4. Experimental Section

Surface Charge Density Characterization: As-purchased FEP, nylon 66, Nafion 211, and FAA-3 films with a 10 × 10 mm dimension were washed with ethanol three times to remove the precharges, followed by mild annealing at 80 °C overnight. A single contact was conducted using a pushing tester (Junil Tech. JIPT-120) housed in a digitalized humidity controller (Terra Universal 1911–24D). The FEP film on indium tin oxide (ITO) was brought into the single contact with nylon 66, Nafion 211, or FAA-3 film at room temperature, and then was annealed at the target temperature (120, 160, or 200 °C) for the desired time. After the desired time, the FEP sample was cooled down to room temperature to measure the trace surface charge, followed by heating again to monitor the trace surface charge as a function of time. The charge of FEP in contact with a copper electrode was measured by Keithley 6514 electrometer, and the compressive load of 0.98 N was chosen to minimize the contact electrification between FEP and copper (the charge transfer derived by the contact electrification was measured to be below 0.1 μC m^{-2}). The surface charge on FEP layer was determined by the following equation:[61]

$$\sigma = \sigma' \left(t_1\varepsilon_2 + d'\varepsilon_2 + t_2\varepsilon_1/t'\varepsilon_1\varepsilon_2\right) \quad (5)$$

where σ and σ' are the surface and induced charges, respectively. The ϵ_1 and ϵ_2 represent the dielectric constants of each contact electrification layer. The t_1 and t_2 denote the thickness of each contact electrification layer. The d' is the separation distance between contact electrification layers. As the dielectric constant of copper is infinite, it was assumed that the surface and induced charges are identical throughout the experiment. All measurements were conducted at 25 ± 2 °C. After we collected the data for the surface charges on the FEP layer as a function of heating time, the decay curve of the surface charge was modeled by electron thermionic emission theory[20,44–47] as shown in Equation (1). The plateau of the decay curve is the measure of surface charge mediated by sticky charge, while the decaying part corresponds to the surface charge mediated by the electron. All charge values are normalized by the initial charge ($\sigma(t = 0)$), and the sign convention for normalized charge indicates the polarity of surface charge.

Intrinsic Ion Charge Density on Ionomer Surfaces Estimation: To estimate the surface ion concentration, a random distribution of the ions and repeating units was assumed. Given that the surface is assumed to be the ions and repeating units occupying 5 Å, the ion charge density ($\sigma_{surface}$) can be approximated by the following equation.

$$\sigma_{surface} = \frac{C}{m} \times N_A \times q \times \rho \times \frac{5\ \forall}{t} \quad (6)$$

where C and m are ion capacity and molar mass of ion, respectively. The ion capacities of Nafion 211 and FAA-3 are 0.98[62] and 1.85[63] meq g^{-1}, respectively. The N_A, q, and ρ are Avogadro's number, elementary charge, and film density, respectively. The t is the film thickness.

Surface Characterization: The trace element detection on the FEP surface in contact with a cationic polymer was carried out using PHI nano Time-of-Flight II Secondary Ion Mass Spectrometry system equipped with Bi_3^{++} primary ion source with an energy and ion current of 30 keV and 2nA, respectively. The raster size of the FEP surface was 600 × 600 μm^2, and the measurement was performed for 15 min under high mass resolution mode for each sample. Furthermore, the surface potential was characterized using a Kelvin probe force microscopy (KPFM, Bruker Dimension Icon). A conductive Bruker SCM-PIT-V2 tip was used in non-contact mode for surface potential measurement, with a scanning area of 20 × 20 μm^2. The potential difference between the tip and a standard Au sample was measured before each measurement to determine the potential of the tip. The operation conditions during the KPFM measurement were: temperature = 22 °C, relative humidity = 30%, 40%, 50%, 60%, and 70% (wait for at least 30 min after reaching the target humidity before the measurement).

TENG Device Fabrication and Characterization: The 50 μm FEP film was cut into the size of 10 mm × 10 mm, followed by pasted on an ITO glass, in which FEP and ITO serve as contact electrification layer and electrode, respectively. The nylon, Nafion 211, and FAA-3 films were also cut into 10 mm × 10 mm pieces and then were attached to a copper tape. The all films were washed three times with ethanol and then was dried and stored in a 80 °C oven overnight. The FEP/ITO and polymers/Cu were tightly fixed on stator and mover of programmed pushing tester, respectively, which is accommodated in the digitalized humidity controller. The initial gap between the FEP and the polymer layers was set to be 20 mm, and the periodic compressive load of 9.8 N with a frequency of 0.36 Hz was subjected to the samples. An oscilloscope (Agilent DSO-X-2014A) equipped with a preamplifier (SRS SR-570) was used for voltage and current measurements. The oxygen plasma treatments to non-ionic polymers were performed in a plasma cleaner (PI-5S Plasma Cleaner, Shenzhen Sanhe Boda Electromechanical Technology Co., Ltd., Shenzhen, China) with a plasma power of 180 W for 2 min.

Moisture Uptake Characterization: The weight change of the Nafion and FAA-3 films after moisture uptake was measured using semi-microbalance (Sartorius Cubis(R) II MCA125S-2S00-I). All tests were conducted at 25 ± 2 °C if no specific explanation existed.

Density Functional Theory (DFT) Computation: The DFT calculations were performed based on the ORCA program package (program 5.0.4).[64] Briefly, the semiempirical method B97-3c basis set was used to optimize the initial structures of Nafion 211 molecule and FAA-3 molecule,[65] and then the water molecules of varying numbers from 1 to 6 were introduced into the above structure to simulate the situations of under different humidity. In order to further obtain a more reliable structure, r2SCAN-3c basis set was used for the next step of optimization.[66] The structures were built and visualized using Avogadro 1.2.0. and built-in measurement tools were used to measure the distance between optimized molecules and protons or bromide anions. To speed up the calculation, resolution of the identity approximation was applied in all processes. All structures were subjected to frequency analysis to ensure the absence of imaginary frequency, indicating that the optimized structures are at the energy minimum point. For final binding energy calculation, we calculated the energies of different groups using ωB97M-V functional[67] and the def2-TZVP basis set.[68] The binding energies were calculated by following formula:

$$E_{binding} = E_{total} - (E_{molecule} + E_{water}) \quad (7)$$

where the E_{total}, $E_{molecule}$, and E_{water} are the whole systems energy, the molecule energy, and the water group energy, respectively.

Molecular Dynamics (MD) Simulations: The MD simulations were performed with Materials Studio. The Condensed-Phase Optimized Molecular Potentials for Atomistic Simulation Studies (COMPASSIII) force field[69] was used to simulate interatomic interactions. Simulations were carried out using the isothermal-isobaric ensemble for equilibration. The pressure was controlled by the Andersen barostat[70] while the temperature was controlled by the Berendsen thermostat.[71] Unless otherwise specified, a time step of 1 fs was used for all simulations. The Ewald summation was used for electrostatic interactions and the atom-based summation with a cut-off distance of 12.5 Å was used for Van der Walls interactions. The initial simulation structures were built by Materials visualizer which is embedded inside the software. The corresponding Nafion 211 and FAA-3 chains were filled in a simulation cell with a size of ≈45 by 45 Å according to the experimental density with periodic boundary conditions

applied along the x- and y- directions, respectively. In order to simulate the experimentally measured humidity state, different proportions of water molecules are introduced into the simulation cell. After the first equilibration, in order to achieve ion equilibrium, annealing procedures were employed. The systems were carried out from 298 K to 600 K 5 times, with each interval of 50 K lasting 100 ps.

In order to study the effectiveness of the proton and bromide anion transportation, the mean square displacement (MSD) method was carried out to investigate the movements.[72] Both interface and inside-materials structures were analyzed. The MSD analysis was performed on the vertical direction of the interface structures while the normal MSD analysis was used for inside-materials structures. The MSD can be obtained from the position change of particles in unit time in a molecular dynamics (MD) simulation by the following equation:

$$MSD = \frac{1}{\tau - \Delta t} \int_0^{\tau - \Delta t} [r(t - \Delta t) - r(t)]^2 dt \quad (8)$$

where τ represents the total production time and $r(t)$ is the position at time t. The increase of MSD with time is related to the diffusion coefficient D as below:

$$D = \frac{1}{6N\alpha} \lim_{t \to \infty} \frac{d}{dt} \sum_{i=1}^{N\alpha} \{[r_i(t) - r_i(0)]\}^2 \quad (9)$$

where N_α is the number of diffusive atoms in the system.

Supporting Information

Supporting Information is available from the Wiley Online Library or from the author.

Acknowledgements

The authors acknowledge the financial support of the Early Career Scheme (Award No. 27202920), General Research Fund (Award No. 17201721), Collaborative Research Fund (Award No. C6047-23G) of the Research Grants Council of the Hong Kong Special Administrative Region, China.

Conflict of Interest

The authors declare no conflict of interest.

Author Contributions

X.M. and J.Z. contributed equally to this work. D.-M.S. and X.M. conceived the overall research goals and aims. D.-M.S. and X.M. designed the experiments. X.M. fabricated devices and performed the characterization with help from J.Z., E.K. and J.G., W.H., D.-M.S. and X.M. performed the data analysis and organized the results. J.Z. developed the molecular dynamics simulations model in this manuscript. All the authors contributed to writing the manuscript.

Data Availability Statement

The data that support the findings of this study are available from the corresponding author upon reasonable request.

Keywords

contact-electrification, energy harvesting, ionic charge transfer, ionomers

Received: March 17, 2025
Revised: July 13, 2025
Published online:

[1] P. Iversen, D. J. Lacks, *J. Electrostat.* **2012**, *70*, 309.
[2] D. M. Pai, B. E. Springett, *Rev. Mod. Phys.* **1993**, *65*, 163.
[3] A. Jaworek, A. T. Sobczyk, *J. Electrostat.* **2008**, *66*, 197.
[4] S. Sahoo, H. Ouyang, J. C. H. Goh, T. E. Tay, S. L. Toh, *Tissue Eng.* **2006**, *12*, 91.
[5] B. A. Kwetkus, *Part. Sci. Technol.* **1998**, *16*, 55.
[6] C. Liu, A. J. Bard, *Nat. Mater.* **2008**, *7*, 505.
[7] C.-y. Liu, A. J. Bard, *J. Am. Chem. Soc.* **2009**, *131*, 6397.
[8] F.-R. Fan, Z.-Q. Tian, Z. Lin Wang, *Nano Energy* **2012**, *1*, 328.
[9] A. Berbille, X.-F. Li, Y. Su, S. Li, X. Zhao, L. Zhu, Z. L. Wang, *Adv. Mater.* **2023**, *35*, 2304387.
[10] T. Lv, R. Cheng, C. Wei, E. Su, T. Jiang, F. Sheng, X. Peng, K. Dong, Z. L. Wang, *Adv. Energy Mater.* **2023**, *13*, 2301178.
[11] X. Liang, S. Liu, S. Lin, H. Yang, T. Jiang, Z. L. Wang, *Adv. Energy Mater.* **2023**, *13*, 2300571.
[12] Z. Deng, L. Xu, H. Qin, X. Li, J. Duan, B. Hou, Z. L. Wang, *Adv. Mater.* **2022**, *34*, 2205064.
[13] Y.-J. Kim, J. Lee, J.-H. Hwang, Y. Chung, B.-J. Park, J. Kim, S.-H. Kim, J. Mun, H.-J. Yoon, S.-M. Park, S.-W. Kim, *Adv. Mater.* **2023**, *36*, 2307194.
[14] M. Kang, D.-M. Lee, I. Hyun, N. Rubab, S.-H. Kim, S.-W. Kim, *Chem. Rev.* **2023**, *123*, 11559.
[15] D. Choi, Y. Lee, Z.-H. Lin, S. Cho, M. Kim, C. K. Ao, S. Soh, C. Sohn, C. K. Jeong, J. Lee, M. Lee, S. Lee, J. Ryu, P. Parashar, Y. Cho, J. Ahn, I.-D. Kim, F. Jiang, P. S. Lee, G. Khandelwal, S.-J. Kim, H. S. Kim, H.-C. Song, M. Kim, J. Nah, W. Kim, H. G. Menge, Y. T. Park, W. Xu, J. Hao, et al., *ACS Nano* **2023**, *17*, 11087.
[16] X. Ma, E. Kim, J. Zhou, J. Gao, C. Kim, X. Huan, J. T. Kim, D.-M. Shin, *Nano Energy* **2023**, *113*, 108589.
[17] J. Jeong, S. Jeon, X. Ma, Y. W. Kwon, D.-M. Shin, S. W. Hong, *Adv. Mater.* **2021**, *33*, 2102530.
[18] S. Im, E. Frey, D. J. Lacks, J. Genzer, M. D. Dickey, *Adv. Sci.* **2023**, *10*, 2304459.
[19] D. J. Lacks, T. Shinbrot, *Nat. Rev. Chem.* **2019**, *3*, 465.
[20] C. Xu, Y. Zi, A. C. Wang, H. Zou, Y. Dai, X. He, P. Wang, Y.-C. Wang, P. Feng, D. Li, Z. L. Wang, *Adv. Mater.* **2018**, *30*, 1706790.
[21] J. Lowell, *J. Phys. D: Appl. Phys.* **1975**, *8*, 53.
[22] W. R. Harper, G. P. Thomson, *Proc. R. Soc. London, Ser. A* **1951**, *205*, 83.
[23] H. A. Mizes, E. M. Conwell, D. P. Salamida, *Appl. Phys. Lett.* **1990**, *56*, 1597.
[24] A. F. Diaz, D. Wollmann, D. Dreblow, *Chem. Mater.* **1991**, *3*, 997.
[25] L. S. McCarty, A. Winkleman, G. M. Whitesides, *Angew. Chem., Int. Ed.* **2007**, *46*, 206.
[26] L. S. McCarty, G. M. Whitesides, *Angew. Chem., Int. Ed.* **2008**, *47*, 2188.
[27] L. S. McCarty, A. Winkleman, G. M. I. E.: Whitesides, *J. Am. Chem. Soc.* **2007**, *129*, 4075.
[28] W. R. Salaneck, A. Paton, D. T. Clark, *J. Appl. Phys.* **2008**, *47*, 144.
[29] J. Lowell, *J. Phys. D: Appl. Phys.* **1977**, *10*, L233.
[30] H. T. Baytekin, A. Z. Patashinski, M. Branicki, B. Baytekin, S. Soh, B. A. Grzybowski, *Science* **2011**, *333*, 308.
[31] R. K. Pandey, H. Kakehashi, H. Nakanishi, S. Soh, *J. Phys. Chem. C* **2018**, *122*, 16154.
[32] O. Verners, L. Lapčinskis, P. C. Sherrell, A. Šutka, *Adv. Mater. Interfaces* **2023**, *10*, 2300562.
[33] A. Šutka, L. Lapcinskis, D. He, H. Kim, J. D. Berry, J. Bai, M. Knite, A. V. Ellis, C. K. Jeong, P. C. Sherrell, *Adv. Mater. Interfaces* **2023**, *10*, 2300323.

[34] H. T. Baytekin, B. Baytekin, J. T. Incorvati, B. A. Grzybowski, *Angew. Chem., Int. Ed.* **2012**, *51*, 4843.
[35] Z. L. Wang, A. C. Wang, *Mater. Today* **2019**, *30*, 34.
[36] Y. S. Zhou, S. Li, S. Niu, Z. L. Wang, *Nano Res.* **2016**, *9*, 3705.
[37] H. Ryu, J.-H. Lee, T.-Y. Kim, U. Khan, J. H. Lee, S. S. Kwak, H.-J. Yoon, S.-W. Kim, *Adv. Energy Mater.* **2017**, *7*, 1700289.
[38] L. Shi, S. Dong, H. Xu, S. Huang, Q. Ye, S. Liu, T. Wu, J. Chen, S. Zhang, S. Li, X. Wang, H. Jin, J. M. Kim, J. Luo, *Nano Energy* **2019**, *64*, 103960.
[39] A. F. Diaz, *J. Adhes.* **1998**, *67*, 111.
[40] D. Fenzel-Alexander, P. Brock, A. Diaz, *Langmuir* **1994**, *10*, 3323.
[41] H. Zhang, S. Sundaresan, M. A. Webb, *Nat. Commun.* **2024**, *15*, 2616.
[42] H. Zou, Y. Zhang, L. Guo, P. Wang, X. He, G. Dai, H. Zheng, C. Chen, A. C. Wang, C. Xu, Z. L. Wang, *Nat. Commun.* **2019**, *10*, 1427.
[43] H. Zou, L. Guo, H. Xue, Y. Zhang, X. Shen, X. Liu, P. Wang, X. He, G. Dai, P. Jiang, H. Zheng, B. Zhang, C. Xu, Z. L. Wang, *Nat. Commun.* **2020**, *11*, 2093.
[44] S. Lin, L. Xu, A. C. Wang, Z. L. Wang, *Nat. Commun.* **2020**, *11*, 399.
[45] J. Ekar, S. Kos, J. Kovač, *Surfaces and interfaces* **2024**, *49*, 104408.
[46] V. Karki, M. Singh, *Int. J. Mass Spectrom.* **2018**, *430*, 22.
[47] M. Grasserbauer, *J. Res. Natl. Bur. Stand.* **1988**, *93*, 510.
[48] P. Van der Heide, *Secondary Ion Mass Spectrometry: An Introduction to Principles and Practices*, John Wiley & Sons, New Jersey **2014**, pp. 248–268.
[49] H. Satoh, M. O. M. Owari, Y. N. Y. Nihei, *Jpn. J. Appl. Phys.* **1993**, *32*, 3616.
[50] R. G. Wilson, *Int. J. Mass Spectrometry. Ion Proc.* **1995**, *143*, 43.
[51] M. Collin, S. Gin, P. Jollivet, L. Dupuy, V. Dauvois, L. Duffours, *npj Mater. Degradation* **2019**, *3*, 14.
[52] C. Xu, B. Zhang, A. C. Wang, W. Cai, Y. Zi, P. Feng, Z. L. Wang, *Adv. Funct. Mater.* **2019**, *29*, 1903142.
[53] X. Xia, H. Wang, H. Guo, C. Xu, Y. Zi, *Nano Energy* **2020**, *78*, 105343.
[54] X. Xia, H. Wang, Y. Zi, *SmartMat* **2022**, *3*, 619.
[55] G. Grosjean, S. Waitukaitis, *Phys. Rev. Lett.* **2023**, *130*, 098202.
[56] A. Šutka, K. Malnieks, L. Lapcinskis, P. Kaufelde, A. Linarts, A. Berzina, R. Zabels, V. Jurkans, I. Gornevs, J. Blums, M. Knite, *Energy Environ. Sci.* **2019**, *12*, 2417.
[57] Y. S. Zhou, Y. Liu, G. Zhu, Z.-H. Lin, C. Pan, Q. Jing, Z. L. Wang, *Nano Lett.* **2013**, *13*, 2771.
[58] D. R. Finley, HSP Color Model — Alternative to HSV (HSB) and HSL. https://alienryderflex.com/hsp.html (accessed: July 2025).
[59] Y. Liu, J. Mo, Q. Fu, Y. Lu, N. Zhang, S. Wang, S. Nie, *Adv. Funct. Mater.* **2020**, *30*, 2004714.
[60] S. Pence, V. J. Novotny, A. F. Diaz, *Langmuir* **1994**, *10*, 592.
[61] S. Niu, Y. Liu, S. Wang, L. Lin, Y. S. Zhou, Y. Hu, Z. L. Wang, *Adv. Funct. Mater.* **2014**, *24*, 3332.
[62] DuPont, DuPont™ Nafion® PFSA Membranes NRE-211 and NRE-212, **2006**, http://www.hesen.cn/userfiles/bochi/file/212%E3%80%81211%E5%8F%82%E6%95%B0.pdf.
[63] FUELCELL Store, fumasep® FAA-3-50, https://www.fuelcellstore.com/spec-sheets/fumasep-faa-3-50-technical-specifications.pdf.
[64] F. Neese, F. Wennmohs, U. Becker, C. Riplinger, *J. Chem. Phys.* **2020**, *152*, 224108.
[65] J. G. Brandenburg, C. Bannwarth, A. Hansen, S. Grimme, *J. Chem. Phys.* **2018**, *148*, 064104.
[66] S. Grimme, A. Hansen, S. Ehlert, J.-M. Mewes, *J. Chem. Phys.* **2021**, *154*, 064103.
[67] N. Mardirossian, M. Head-Gordon, *J. Chem. Phys.* **2016**, *144*, 214110.
[68] F. Weigend, R. Ahlrichs, *Phys. Chem. Chem. Phys.* **2005**, *7*, 3297.
[69] H. Sun, *J. Phys. Chem. B* **1998**, *102*, 7338.
[70] G. J. Martyna, D. J. Tobias, M. L. Klein, *J. Chem. Phys.* **1994**, *101*, 4177.
[71] H. J. C. Berendsen, J. P. M. Postma, W. F. van Gunsteren, A. DiNola, J. R. Haak, *J. Chem. Phys.* **1984**, *81*, 3684.
[72] Q. Xue, C. Lv, M. Shan, H. Zhang, C. Ling, X. Zhou, Z. Jiao, *Comput. Mater. Sci* **2013**, *71*, 66.